nature geoscience

ARTICLES

https://doi.org/10.1038/s41561-018-0089-5

Chilean megathrust earthquake recurrence linked to frictional contrast at depth

M. Moreno[1,2*], S. Li[1,3], D. Melnick[4,5], J. R. Bedford[1], J. C. Baez[6], M. Motagh[1,7], S. Metzger[1], S. Vajedian[7], C. Sippl[1], B.D. Gutknecht[8], E. Contreras-Reyes[9], Z. Deng[1], A. Tassara[5,10] and O. Oncken[1]

Fundamental processes of the seismic cycle in subduction zones, including those controlling the recurrence and size of great earthquakes, are still poorly understood. Here, by studying the 2016 earthquake in southern Chile—the first large event within the rupture zone of the 1960 earthquake (moment magnitude (M_w) = 9.5)—we show that the frictional zonation of the plate interface fault at depth mechanically controls the timing of more frequent, moderate-size deep events ($M_w < 8$) and less frequent, tsunamigenic great shallow earthquakes ($M_w > 8.5$). We model the evolution of stress build-up for a seismogenic zone with heterogeneous friction to examine the link between the 2016 and 1960 earthquakes. Our results suggest that the deeper segments of the seismogenic megathrust are weaker and interseismically loaded by a more strongly coupled, shallower asperity. Deeper segments fail earlier (~60 yr recurrence), producing moderate-size events that precede the failure of the shallower region, which fails in a great earthquake (recurrence >110 yr). We interpret the contrasting frictional strength and lag time between deeper and shallower earthquakes to be controlled by variations in pore fluid pressure. Our integrated analysis strengthens understanding of the mechanics and timing of great megathrust earthquakes, and therefore could aid in the seismic hazard assessment of other subduction zones.

Models of recent, large, subduction-zone earthquakes have revealed spatial relations between zones of high pre-seismic locking on the interface and regions of large coseismic slip, mechanically indicative of so-called asperities[1–5]. Although such relationships can be interpreted as evidence for heterogeneous fault friction properties[3,6], little is known about the physical controls on the spatial distribution of creep, locking and slip on a seismogenic interface. Possible hypotheses include the varying degrees of geometric complexity[7,8], the nature and thickness of the trench sediments[9], variable fluid release at different depths[10–13], differential loading along the plate interface associated with the geologic structure of the upper plate[14–16] and fault zone rheology[17,18]. Each of these proposed physical mechanisms may independently influence dynamic, mechanical, and hydraulic properties of the subduction interface and consequently its frictional strength (stress required to initiate earthquake slip) and kinematics.

The lack of precision and completeness in deformation records between great earthquakes, and the rarity in recording major events affecting the same segment have restricted the characterization of the earthquake cycle to short snapshots. Thus, our understanding of the cycle in terms of frictional conditions along the plate interface is limited. The 25 December 2016 southern Chile earthquake[19] (moment magnitude (M_w) = 7.6; Fig. 1) is the first sign of seismic reactivation within the segment that failed during the 1960 megathrust earthquake—the largest recorded by modern seismology[20,21]. Therefore, exploring the relationship between both events could provide insights into the persistence of asperities and a better understanding of slip behaviour (locking, creeping and seismic slip) with respect to spatiotemporal variations in frictional properties on the plate interface.

The 2016 Southern Chile earthquake

The first-order kinematics of the 2016 event[19] resembles previous Chilean megathrust events (that is, 1985 Central Chile[22], 1995 Antofagasta[23], 2007 Tocopilla[24]) in that most slip occurred along the deeper portions of the seismogenic region of the megathrust, within the transitional rheological separation to aseismic sliding[25,26]. Furthermore, such deeper, zone-C events[26] with M_w = 7–8 are more frequent than great ($M_w > 8.5$) shallower events in subduction zones[27] and thus play an important role in the process of stress build-up and release of seismic energy.

The 2016 earthquake ruptured the deeper portion of an area thought to represent a locked asperity, based on decadal-scale geodetic monitoring[28] (Fig. 1). Kinematic models suggest that this patch previously released its full slip deficit in 1960 with over 10 m of slip[29]. We report near-fault, static surface displacements of the 2016 mainshock recorded by nine continuous GPS stations and synthetic aperture radar (SAR) differential interferograms (Fig. 1b and Supplementary Figs. 1–4). The largest recorded horizontal and vertical displacements occurred at Guafo Island (located ~20 km from the epicentre). To derive the slip distribution, we jointly inverted the GPS and InSAR data. Our preferred slip solution (Fig. 1) suggests a simple rupture composed of a single slip patch with a maximum slip of 2.9 m at 22 km depth. This amount is consistent with the release of ~80% of the total plate motion accumulated there since 1960.

[1]GFZ Helmholtz Centre Potsdam, German Research Centre for Geosciences, Telegrafenberg, Potsdam, Germany. [2]Departamento de Geofísica, Facultad de Ciencias Físicas y Matemáticas, Universidad de Concepción, Concepción, Chile. [3]Department of Earth and Environmental Sciences, University of Iowa, Iowa City, IA, USA. [4]Instituto de Ciencias de la Tierra, TAQUACH, Universidad Austral de Chile, Valdivia, Chile. [5]Millennium Nucleus The Seismic Cycle Along Subduction Zones, Valdivia, Concepción, Chile. [6]Centro Sismológico National, Universidad de Chile, Facultad de Ciencias Físicas y Matemáticas, Santiago, Chile. [7]Institute of Photogrammetry and GeoInformation, Leibniz Universität Hannover, Hannover, Germany. [8]Institut für Planetare Geodäsie, Technische Universität Dresden, Dresden, Germany. [9]Departamento de Geofísica, Facultad de Ciencias Físicas y Matemáticas, Universidad de Chile, Santiago, Chile. [10]Departamento de Ciencias de la Tierra, Facultad de Ciencias Químicas, Universidad de Concepción, Concepción, Chile.
*e-mail: marcos@gfz-potsdam.de

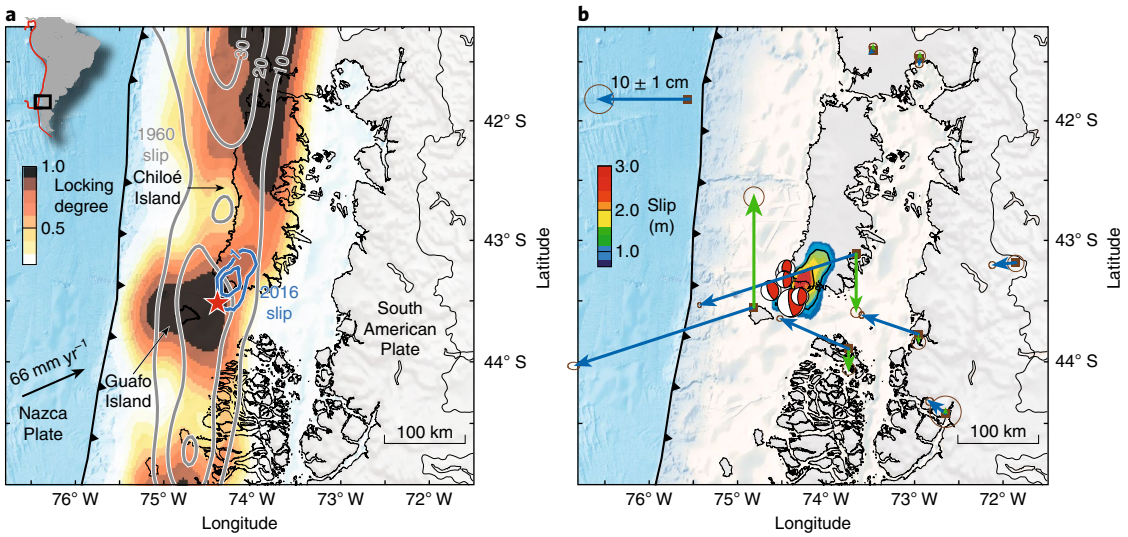

Fig. 1 | The 1960 and 2016 earthquakes. a, The 2016 earthquake affected the southern half of the rupture zone of the 1960 event. White–grey lines show the rupture zone (10 m) of the 1960 earthquake[29]. The red star shows the epicentre of the 2016 event. Blue contours (1 m) depict the slip of the 2016 event. Background colours show the distribution of locking degree[28]. **b**, Slip distribution derived from our joint inversion is shown by a coloured grid. Horizontal and vertical GPS coseismic displacements are shown by blue and green arrows, respectively. Focal mechanisms of the aftershock sequence are plotted in red.

This is in agreement with the degree of pre-2016 locking, implying that the 2016 earthquake released most of the elastic strain accumulated over 56 years in this area. The epicentre and aftershocks of this event were located just up-dip of the zone of highest coseismic slip, similar to the location of the background seismicity recorded before 2016[30] (Fig. 2a). Interestingly, the aftershock sequence featured relatively low magnitudes ($M_w < 5.5$) and event numbers rapidly decayed with time (Supplementary Fig. 6), suggesting the regions surrounding the mainshock were below the critical conditions for failure.

The seismogenic zone in this area has been inferred to be shallow and controlled by a hot and young (13 Ma) incoming Nazca Plate[30]. The seismic to aseismic transition along the interface has been mapped at ~30 km depth and coincides with an isotherm of ~325 °C, close to the tip of the hydrated mantle wedge at the intersection of the slab with the continental Moho[31] (Fig. 2c). Below this limit, neither interseismic microseismicity[30] nor aftershocks of the 2016 event have been recorded, indicating a rheological regime where creep is dominant.

Using offshore multichannel seismic reflection data (Supplementary Fig. 7), we mapped the morphology and distribution of Tertiary forearc basins. We find that Guafo Island lies over a sedimentary basin, which has a thickness of ~750 m at the depocentre. A patch of high interseismic locking and large 1960 slip release is coincident with a region of negative anomalous gravity[32] in the basin area (Fig. 2). The relation between gravity lows (basins) and concentration of coseismic slip (high locking) has been linked with elevated effective coefficients of friction and thus higher shear fault strengths (greater resistance) that cause long-term (million year timescale) topographic depressions[14,33]. The continental basement has a local high (ridge) that delimits the eastern border of the basin. This ridge structure correlates with a relative gravity high, which coincides with the downdip end of the locked zone as well as of the downdip extents of the 1960 and 2016 coseismic ruptures. Such a gravity high has been observed globally along subduction zones[32], and has been inferred to represent an expression of the long-term stability of the downdip limit of the seismogenic zone. Likewise, the ridge structure could be caused by the transformation of interseismic strain into permanent geologic strain via faulting, folding and/or buckling of the inner forearc at the transition between unstable (seismic) and stable (aseismic) sliding[32].

Stress build-up along the seismogenic zone

Heterogeneity in frictional strength at the plate interface is a first-order control on earthquake rupture and frequency[34]. The spatial correlation between the forearc structure and the kinematics of both the 1960 and 2016 events suggests a depth-varying frictional segmentation along the seismogenic zone (Fig. 2c), with the shallower segment being the highly coupled portion of the fault (higher shear strength state at depths shallower than 20 km), and the deeper segment localized in the narrow transition from unstable to stable slip (the rupture zone of 2016 event at 20–30 km depth).

Inspired by the observed correlation, we investigated the frictional structure of the seismogenic zone with a mechanical model designed to simulate the evolution of stress build-up due to the steady subduction[35] of a coupled asperity under the Coulomb friction failure criterion. Our model outputs the spatiotemporal evolution of tractions (stresses on the fault plane) for a heterogeneous frictional seismogenic zone under tectonic stress loading. We do not attempt to model the complex dynamics of rupture[6,36] and subsequent healing[37], which are of short duration compared with the period of stress build-up of a 2016-class earthquake (56 yr assuming that the 1960 event released all stress in the 2016 zone). In our model, a higher coefficient of effective friction clamps a segment of the fault (no sliding) until the frictional forces overcome the fault strength and the coupled section begins to slide. Aseismic slip occurs around areas with a lower effective coefficient of friction, where the weaker interface fails due to a smaller resisting shear strength. The clamp model produces a deformation halo of low creep rate surrounding the coupled asperity that in turn causes higher strain rates downdip, effectively loading these areas while shielding updip portions of the asperity (Supplementary Fig. 9) due to the shadowing of stresses[38].

It is important to note that the size of the coupled asperity and the frictional contrast around the asperity control both the pattern of strain energy concentration at the downdip end and the rupture interval (time when a fault segment begins sliding without building extra stress) (Supplementary Fig. 9). Accordingly, larger asperities require more time to reach the critical failure state. We tested a wide range of frictional contrasts based on the distribution of locking degree to define the boundary of the coupled asperity. We found a significant spatial correlation between the shear stress accumulation after 50 yr of interseismic loading in the deeper fault portion and the

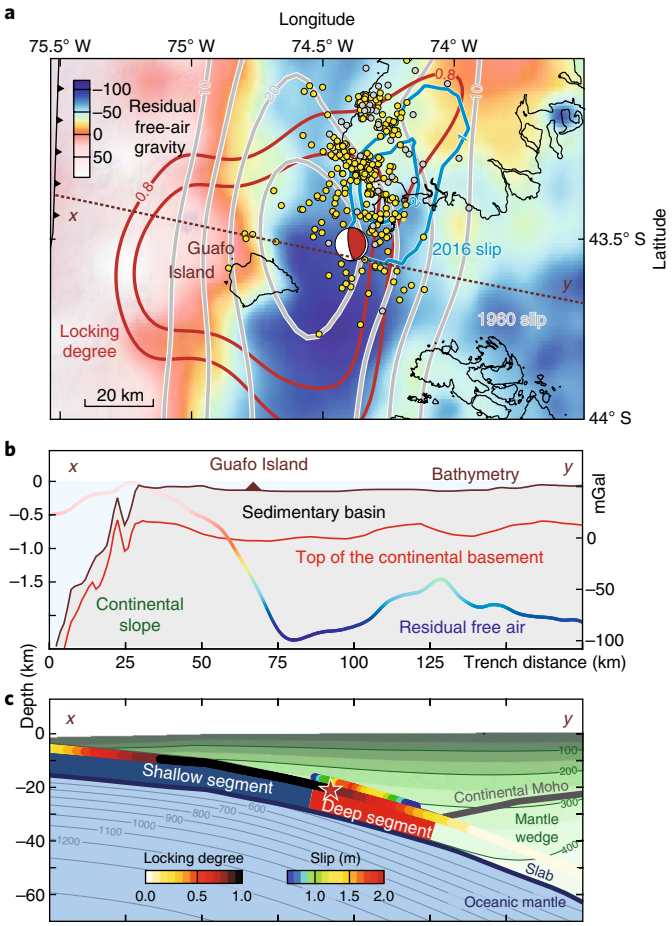

Fig. 2 | Downdip segmentation of the seismogenic zone. a, High locking degree (>0.8, red contours) and large 1960 slip (white–grey 5 m contours) coincides with a region of negative free-air gravity anomaly[32]. The 2016 earthquake (blue 1 m contours) was located below this region. Yellow dots and the red beachball show locations of aftershocks and the mechanism of the 2016 earthquake, respectively. Grey dots show interseismic background seismicity. **b**, Cross-section *xy* showing the forearc morphology and gravity anomaly[32]. **c**, Locking and slip distribution overlaying a thermal model[31]. Shallow (<20 km depth) and deep (20–30 km depth) segments of the plate interface are shown.

slip of the 2016 earthquake when the shallow segment of the fault is clamped (Fig. 3a). This finding suggests that the shallow segment mechanically behaves like a coupled asperity that induces strain and stress accumulation in the deeper seismogenic segment. This is also supported by its kinematics, as this fault section released the highest slip during the 1960 event (slip >25 m) and its centre is fully locked (locking degree >0.9; Fig. 2). Our model shows that following a deeper-class earthquake, the shallower coupled segment will continue stressing and straining the transition between the shallower and deeper segments, but with a reduced ring-shaped area (Fig. 3b). After 100 yr of loading, a subsequent rupture of the entire coupled segment could also drive failure of the down-dip region, producing a $M_w > 8.5$ earthquake.

Failure lag time

Given the lag time between the 1960 and 2016 events, we further investigated the effective friction coefficients for both the shallow and deep fault segments that would favour the rupture of the deep segment after 60 ± 5 yr of interseismic loading. In doing so, we assume that tectonic stress guides the loading of the system and seismic stress drop represents pre-earthquake stress conditions on the fault. In addition, we assume that a giant 1960-class event fully releases the accumulated elastic stresses, as proposed for the 2011 Tohoku earthquake[39]. We focus on characterizing the downdip frictional zonation across the 2016 rupture zone, and thus we do not attempt to explore along-strike variations. The rupture times of the fault segments are assessed as the initial time when the fault cannot hold the accumulated stresses in the system, marking the onset of unstable sliding. The results indicate the range of coefficients of friction combinations (between the shallow and deep segments) that can produce the observed 56-year lag time for rupture of the deep segment (Supplementary Fig. 10). The effective friction coefficient of the deep segment needs to be <0.01 and always lower than that of the shallow segment, which ranges between 0.01 and 0.04 (Supplementary Fig. 10). This result suggests that the seismogenic zone is weak, with an effective friction coefficient of generally <0.04, as suggested by thermal modelling studies[40].

The rupture time of the deep segment depends not only on its own effective friction coefficient but also on the transfer of stress from the shallow segment. Hence, the spatiotemporal evolution of stress build-up, and thus timing of ruptures, can be controlled by the contrast in effective friction between the shallow and deep seismogenic segments (Supplementary Fig. 11). We cannot yet directly establish the value of the friction coefficient of the shallow segment, and therefore its rupture time. We can, however, use the stress drop of the 2016 event (Supplementary Fig. 12) as a proxy for the expected stress in this region. Thus, to accumulate shear stresses in the range of the stress drop after 56 yr of steady subduction, the effective friction coefficient of the deep segment needs to be 30–40% of the value of the shallow segment (Fig. 4a). We can narrow the rupture time of the shallow segment to an optimal range of 110–140 yr of interseismic loading (Fig. 4a), similar to the recurrence time of historical $M_w > 8$ ruptures[41]. The proposed differential along-dip mechanical behaviour of the seismogenic zone allows an elastic slip deficit accumulation period on the shallow segment to be twice as long as on the deeper segment; such a longer period may thus result in great tsunamigenic earthquakes.

Frictional contrast and pore pressure relationship

Our model suggests that differences in lithostatic load (Supplementary Fig. 14) alone cannot produce the short-term mechanical behaviour of a coupled asperity. High normal stress couples the fault below the seismogenic limit, whereas low normal stress induces a reduction of fault resistance in the shallow segment, opposite to its mechanical behaviour (Supplementary Fig. 15). Hence, variations on the effective friction coefficient are expected to offset the normal stress[14]. It has long been recognized that pore fluid pressure can counteract the normal stress, weakening the absolute strength and stability of a fault[10,42]. Likewise, gradients in fluid pressure can induce fault strength segmentation[11,13], with drained conditions promoting fault coupling[12,13].

By assuming that the pore fluid pressure gradient is the main parameter varying the frictional resistance, we estimated the values of the pore pressure ratio (λ = pore pressure/lithostatic stress) based on the predicted values of effective friction coefficient (Fig. 4b). We ignored additional factors beside pore pressure alone, such as heterogeneity of the shear zone and accumulation of damage[37], that may play a role in frictional variations. In absence of these additional complexities, our results suggest that λ in the deep segment has to be >0.98 to permit its rupture after ~56 years of loading. In contrast, in the shallow segment $\lambda = 0.95$–0.96 is needed in order to accumulate the shear traction matching the stress drop of the 2016 event. Our results not only support the anti-correlation between locking degree and λ proposed by previous studies[10,12], but also demonstrate that overpressure results in a faster release of shear stress, potentially causing more frequent earthquakes of moderate

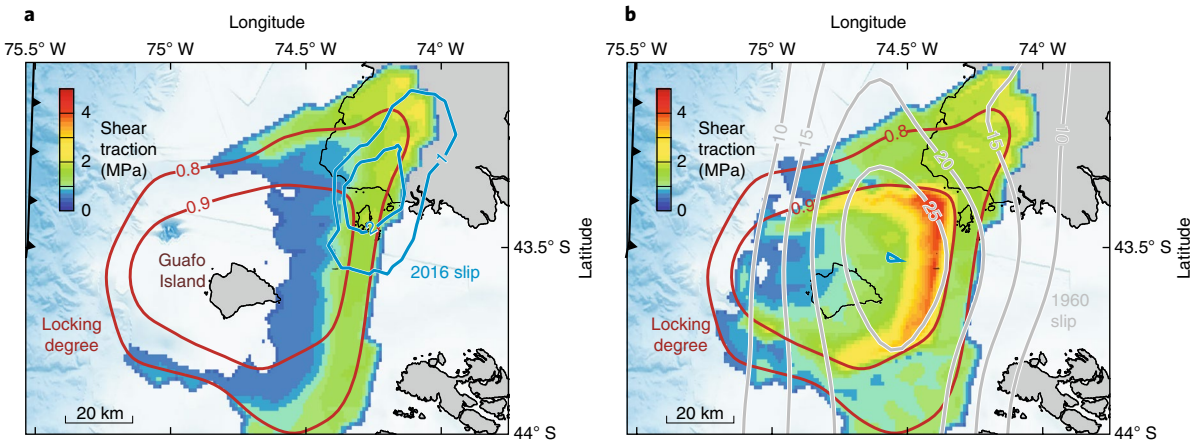

Fig. 3 | Stress build-up pattern around a clamped shallow asperity. This model incorporates an effective friction coefficient of the deep segment 0.35 times the value of the shallow segment. Red contours delimit highly locked areas (>0.8). **a**, Stress build-up after 50 years of loading. This model produces a shear traction accumulation similar in magnitude and location with the rupture zone of the 2016 earthquake (1 m blue contours). **b**, Stress build-up after 100 years of loading. Shear traction is accumulated in the downdip limit of the asperity, encircling the area with highest slip during the 1960 event (white–grey 5 m contours).

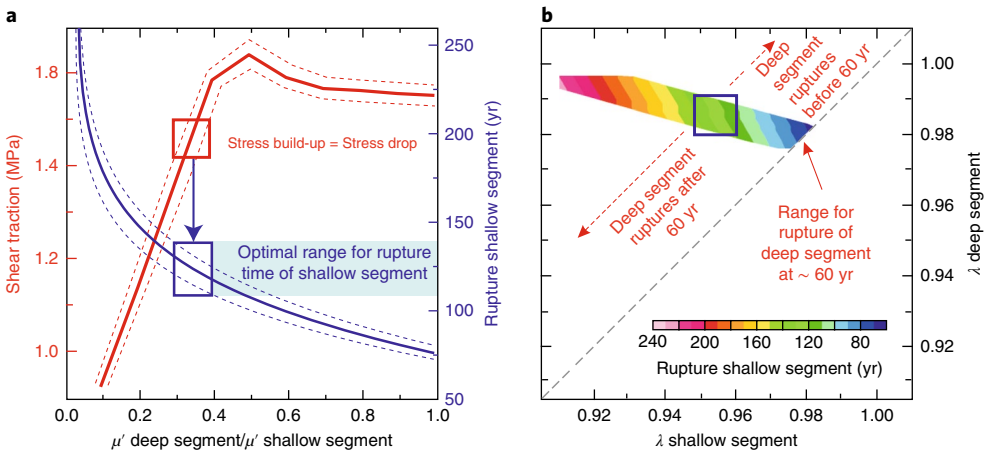

Fig. 4 | Effective friction coefficient and pore pressure ratios. a, Shear traction in the deep segment and rupture time of the shallow segment as functions of the effective friction coefficient (μ') ratio. Red curves show the accumulated shear traction in the deep segment after 60 ± 5 yr of loading. Blue curves show the rupture time of shallow segment with 95% confidence intervals. Stress build-up matches the 2016 stress drop when μ' of the deeper segment is 30–40% of the value of the shallower segment. This frictional contrast suggests a rupture time of 110–140 yr for the shallow segment. **b**, Estimation of pore pressure ratio (λ) for both segments. Rupture times of the shallow segment are given by the colour for possible combinations of λ that should produce the rupture of the deeper segment at 56 yr lag time. The blue square marks the range of λ combinations determined from Fig. 4a.

size. Pore fluid may thus exert similar stresses to the lithostatic load, providing an explanation for the apparent weakness of the fault in the transition between unstable and stable frictional behaviour. In our study area, this transition ends around the slab-Moho discontinuity, where temperatures are inferred to be 300–400 °C (ref. [31]), and where serpentinite and other hydrous minerals may release fluids into the seismogenic zone maintaining pore pressure close to lithostatic values (Fig. 5).

Localized hydration at the base of the continental plate will form an effective permeability seal because of associated volumetric dilation caused by the hydrous mineral phases, forcing fluids to move upwards along the interplate fault zone and increasing pore pressure[43]. In addition, high pore pressures within the plate interface in southern Chile may be partly attributed to its geological history. Here, the forearc basement consists of metamorphic rocks from a Permo–Triassic accretionary complex[44]. Geophysical images and exhumation history suggest rock units exposed at the surface are continuous to interplate depths[44,45] (Fig. 5). These units are associated with duplex structures interpreted to reflect continuous basal accretion of underthrusted trench sediments[44]. Such duplexes are formed by low-angle thrust sheets dominated by subhorizontal foliations. These pervasive structures are locally cut by submetric vertical quartz veins interpreted as syn-exhumation tension gashes filled with silica-rich fluids pumped by seismogenic processes[43,44]. The predominant horizontal fabrics of basally accreted material may constitute an additional permeability seal (stratigraphic fluid barrier) precluding the ascent of trapped fluids, in contrast to intrusive continental framework rocks that are usually associated with vertical cooling fabrics. Subhorizontal fabrics in southern Chile may thus play a role in restricting vertical fluid migration pathways and enhancing interplate pore pressure.

The interseismic GPS deformation field shows a landward reduction from 50 mm yr^{-1} to 12 mm yr^{-1} in a distance of only 100 km, indicating a high degree of crustal shortening just above the deeper

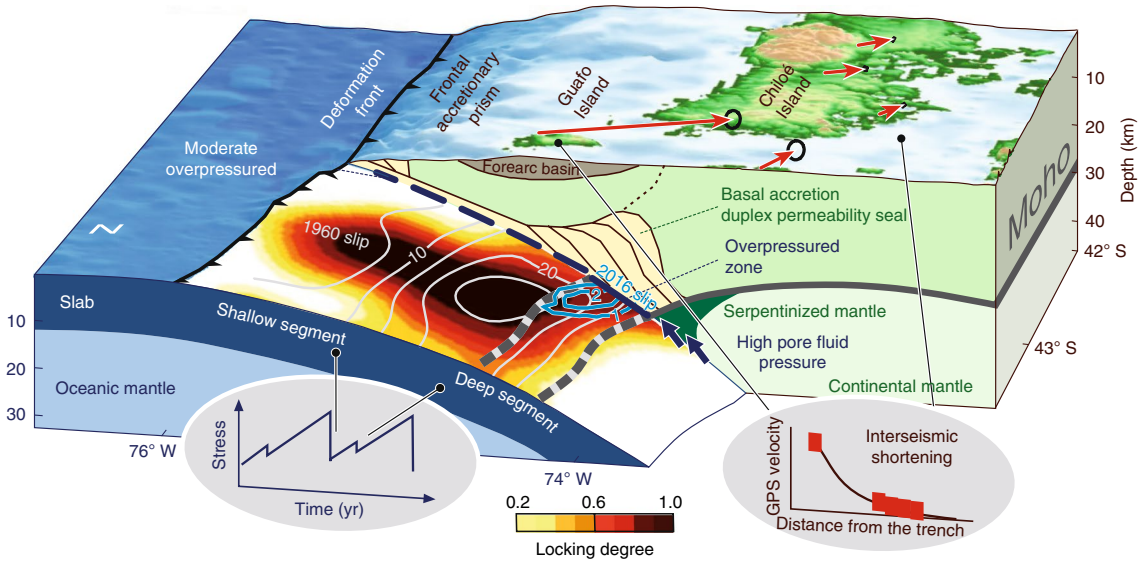

Fig. 5 | Schematic conceptual model of the frictional loading across the plate interface. The stronger shallower segment strains and stresses the deeper segment of the seismogenic zone. The deeper segment is weaker and fails at lower stress build-up in 2016-class earthquakes. Higher shear strength along the shallow segment allows longer periods (>110 yr) of stress build-up, the release of which may result in great 1960-class earthquakes that can also extend into the deeper segment. Interseismic GPS velocities indicate high crustal shortening above the deeper section of the seismogenic zone (right inset). Pore fluid pressure gradients along the plate interface are related to the geological configuration of the margin, and exert a mechanical control on the strength segmentation and timing of stress release in the seismogenic zone (left inset).

section of the seismogenic zone (Fig. 5). This observation corroborates our conceptual model of the deeper segment being interseismically strained. This mechanical behaviour appears to have a major impact on the long-term morphology of subduction margins as suggested by the relation of forearc basins with seismic asperities[14–16] and the permanent emergence of coastlines above deeper seismogenic segments[46].

In summary, we propose that a variation in pore fluid pressure induces a downdip zonation of frictional strength along the plate interface. The frictional contrast at depth may thus control the lag time between deeper seismic ruptures (such as the 2016 event) and great shallower megathrust earthquakes (such as the 1960 event). Hence, deeper 2016-class earthquakes may be considered as a first phase of energy release that precedes failure of the shallower region during great earthquakes. Rupture of the shallow segment could drive failure of the downdip region even if the latter has experienced more-frequent smaller events, resulting in a 1960-class earthquake. Although our model assumes uniform properties along-strike, in nature the frictional contrast may vary along strike, making the failure time different at different along-strike segments. The central part of the 1960 rupture zone seems to be highly locked[28] in a wider along-strike segment than in the 2016 region. This suggests that either the fault strength is uniform over a larger along-strike segment or that the friction contrast at depth is relatively low, allowing a bigger area to be clamped over a longer period. Our model predicts that as interseismic strain builds up, more 2016-class events should occur along the 1960 rupture zone. These forthcoming events will allow a better understanding of along-strike frictional variations. Further development of this modelling strategy, such as incorporating variations of frictional behaviour in the strike direction, could be used to estimate the critical failure threshold of asperities and their time-dependent seismic potential.

Methods

Methods, including statements of data availability and any associated accession codes and references, are available at https://doi.org/10.1038/s41561-018-0089-5.

Received: 10 August 2017; Accepted: 27 February 2018;
Published online: 02 April 2018

References

1. Bürgmann, R. et al. Interseismic coupling and asperity distribution along the Kamchatka subduction zone. *J. Geophys. Res.* **110**, B07405 (2005).
2. Chlieh, M., Avouac, J., Sieh, K., Natawidjaja, D. & Galetzka, J. Heterogeneous coupling of the Sumatran megathrust constrained by geodetic and paleogeodetic measurements. *J. Geophys. Res.* **113**, B05305 (2008).
3. Perfettini, H. et al. Seismic and aseismic slip on the Central Peru megathrust. *Nature* **465**, 78–81 (2010).
4. Moreno, M., Rosenau, M. & Oncken, O. Maule earthquake slip correlates with pre-seismic locking of Andean subduction zone. *Nature* **467**, 198–202 (2010).
5. Loveless, J. P. & Meade, B. Spatial correlation of interseismic coupling and coseismic rupture extent of the 2011 M_w=9.0 Tohoku-oki earthquake. *Geophys. Res. Lett.* **38**, L17306 (2011).
6. Kaneko, Y., Avouac, J. & Lapusta, N. Towards inferring earthquake patterns from geodetic observations of interseismic coupling. *Nat. Geosci.* **3**, 363–369 (2010).
7. Wang, K. & Bilek, S. Do subducting seamounts generate or stop large earthquakes? *Geology* **39**, 819–822 (2011).
8. Kopp, H. Invited review paper: the control of subduction zone structural complexity and geometry on margin segmentation and seismicity. *Tectonophysics* **589**, 1–16 (2013).
9. Ruff, L. Do trench sediments affect great earthquake occurrence in subduction zones? *PAGEOPH* **129**, 263–282 (1989).
10. Saffer, D. M. & Tobin, H. J. Hydrogeology and mechanics of subduction zone forearcs: fluid flow and pore pressure. *Annu. Rev. Earth Planet. Sci.* **39**, 157–186 (2011).
11. Audet, P. & Schwartz, S. Hydrologic control of forearc strength and seismicity in the Costa Rican subduction zone. *Nat. Geosci.* **6**, 852–855 (2013).
12. Moreno, M. et al. Locking of the Chile subduction zone controlled by fluid pressure before the 2010 earthquake. *Nat. Geosci.* **7**, 292–296 (2014).
13. Saffer, D. M. Mapping fluids to subduction megathrust locking and slip behavior. *Geophys. Res. Lett.* **44**, 9337–9340 (2017).
14. Song, T. R. A. & Simons, M. Large trench-parallel gravity variations predict seismogenic behavior in subduction zones. *Science* **301**, 630–633 (2003).
15. Wells, R. E., Blakely, R. J., Sugiyama, Y., Scholl, D. W. & Dinterman, P. A. Basin-centred asperities in great subduction zone earthquakes: a link between slip, subsidence, and subduction erosion. *J. Geophys. Res.* **108**, 2507–2537 (2003).

16. Bassett, D., Sandwell, D., Fialko, Y. & Watts, A. Upper-plate controls on co-seismic slip in the 2011 magnitude 9.0 Tohoku-oki earthquake. *Nature* **531**, 92–96 (2016).
17. Angiboust, S. et al. Probing the transition between seismically coupled and decoupled segments along an ancient subduction interface. *Geochem. Geophys. Geosyst.* **16**, 1905–1922 (2015).
18. Gao, X. & Wang, K. Rheological separation of the megathrust seismogenic zone and episodic tremor and slip. *Nature* **543**, 416–419 (2017).
19. Ruiz, S. et al. Reawakening of large earthquakes in south central Chile: the 2016 M_w 7.6 Chiloé, event. *Geophys. Res. Lett.* **44**, 6633–6640 (2017).
20. Plafker, G. & Savage, J. Mechanism of the Chilean earthquake of May 21 and 22, 1960. *Geol. Soc. Am. Bull.* **81**, 1001–1030 (1970).
21. Barrientos, S. & Ward, S. The 1960 Chile earthquake: inversion for slip distribution from surface deformation. *Geophys. J. Int* **103**, 589–598 (1990).
22. Barrientos, S. Slip distribution of the 1985 Central Chile earthquake. *Tectonophysics* **145**, 225–241 (1988).
23. Pritchard, M. E. et al. Geodetic, teleseismic, and strong motion constraints on slip from recent southern Peru subduction zone earthquakes. *J. Geophys. Res.* **112**, B03307 (2007).
24. Motagh, M. et al. Subduction earthquake deformation associated with 14 November 2007, M_w 7.8 Tocopilla earthquake in Chile: results from InSAR and aftershocks. *Tectonophysics* **490**, 66–68 (2010).
25. Schurr, B. et al. The 2007 M7.7 Tocopilla northern Chile earthquake sequence: Implications for along-strike and downdip rupture segmentation and megathrust frictional behavior. *J. Geophys. Res.* **117**, B05305 (2012).
26. Lay, T. et al. Depth-varying rupture properties of subduction zone megathrust faults. *J. Geophys. Res.* **117**, B04311 (2012).
27. Allen, T., Marano, K., Earle, P. & Wald, D. PAGER-CAT: a composite earthquake catalog for calibrating global fatality models. *Seismol. Res. Lett.* **80**, 57–62 (2009).
28. Moreno, M. et al. Heterogeneous plate locking in the South-Central Chile subduction zone: building up the next great earthquake. *Earth Planet. Sci. Lett.* **305**, 413–424 (2011).
29. Moreno, M. S., Bolte, J., Klotz, J. & Melnick, D. Impact of megathrust geometry on inversion of coseismic slip from geodetic data: Application to the 1960 Chile earthquake. *Geophys. Res. Lett.* **36**, L16310 (2009).
30. Lange, D. et al. Seismicity and geometry of the south Chilean subduction zone (41.5°S-43.5°S): Implications for controlling parameters. *Geophys. Res. Lett.* **34**, L06311 (2007).
31. Völker, D., Grevemeyer, I., Stipp, M., Wang, K. & He, J. Thermal control of the seismogenic zone of southern central Chile. *J. Geophys. Res.* **116**, B10305 (2011).
32. Bassett, D. & Watts, A. Gravity anomalies, crustal structure, and seismicity at subduction zones: 1. seafloor roughness and subducting relief. *Geochem. Geophys. Geosyst.* **16**, 1508–1540 (2015).
33. Fuller, C., Willett, S. & Brandon, M. Formation of forearc basins and their influence on subduction zone earthquakes. *Geology* **34**, 65–68 (2006).
34. Scholz, C. H. Earthquakes and friction laws. *Nature* **391**, 37–42 (1998).
35. Kanda, R. & Simons, M. An elastic plate model for interseismic deformation in subduction zones. *J. Geophys. Res.* **115**, B03405 (2010).
36. Perfettini, H. & Ampuero, J. P. Dynamics of a velocity strengthening fault region: Implications for slow earthquakes and postseismic slip. *J. Geophys. Res.* **113**, B09411 (2008).
37. Rice, J., Sammis, C. & Parsons, R. Off-fault secondary failure induced by a dynamic slip pulse. *Bull. Seismol. Soc. Am.* **96**, 109–134 (1995).
38. Hetland, E. A. & Simons, M. Post-seismic and interseismic fault creep ii: transient creep and interseismic stress shadows on megathrusts. *Geophys. J. Int.* **181**, 99–112 (2010).
39. Hasegawa, A., Yoshida, K. & Okada, T. Nearly complete stress drop in the 2011 M_w 9.0 off the Pacific coast of Tohoku Earthquake. *Earth Planet. Sp.* **63**, 35 (2011).
40. Gao, X. & Wang, K. Strength of stick-slip and creeping subduction megathrusts from heat flow observations. *Science* **345**, 1038–1041 (2014).
41. Cisternas, M. et al. Predecessors of the giant 1960 Chile earthquake. *Nature* **437**, 404–407 (2005).
42. K. Hubbert, M. & Rubey, W. Role of fluid pressure in mechanics of overthrust faulting: I. Mechanics of fluid-filled porous solids and its application to overthrust faulting. *Bull. Seismol. Soc. Am.* **70**, 115–166 (1959).
43. Bachmann, R. et al. Exposed plate interface in the European Alps reveals fabric styles and gradients related to an ancient seismogenic coupling zone. *J. Geophys. Res.* **114**, B05402 (2009).
44. Glodny, J. et al. Differential Late Paleozoic active margin evolution in south-central Chile (37-40°S) - the Lanalhue Fault Zone. *J. South Am. Earth Sci.* **26**, 397–4110 (2008).
45. Groß, K., Micksch, U. & Group, T. R. The reflection seismic survey of project TIPTEQ-the inventory of the Chilean subduction zone at 38.2°S. *Geophys. J. Int.* **172**, 565–571 (2007).
46. Melnick, M. Rise of the central Andean coast by earthquakes straddling the Moho. *Nat. Geosci.* **9**, 401–407 (2016).

Acknowledgements

This work is supported by the German Science Foundation (DFG) grants MO3157/2-3 (M.M., J.R.B.) and SCHU2460/3-1 (C.S.), Millennium Scientific Initiative (ICM) grant NC160025 "CYCLO - the seismic cycle along subduction zones" (D.M., A.T.), Chilean National Commission for Scientific and Technological Research (CONICYT) grant PAI-MEC 2016 (M.M.), FONDECYT 1150321 (D.M.), and Helmholtz Graduate Research School GeoSim (S.L.). ALOS original data are copyright of the Japanese Aerospace Exploration Agency and provided under proposal 1161 (M.Mo.).
This study was encouraged by discussions with B. Schurr and I. Urrutia.
We thank Armada de Chile for hosting our cGPS stations GUAF (Faro Guafo) and MELK (Melinka).

Author contributions

M.M. and S.L. conceived the original idea, which was elaborated with J.R.B., D.M. and O.O. M.M. and S.L performed all numerical simulations. J.R.B. performed the slip inversions. S.M., M.Mo. and S.V. processed the InSAR data. J.C.B. and Z.D. processed the GPS data. S.M. performed the time series analysis of GPS data. B.D.G. performed the stress anomaly model. C.S. processed the seismological data. E.C. performed the processing of seismic reflection data. D.M. installed cGPS stations. The manuscript was written by M.M. with comments from D.M., J.R.B., S.L., C.S., S.M., O.O., E.C. and A.T.

Competing interests

The authors declare no competing interests.

Additional information

Supplementary information is available for this paper at https://doi.org/10.1038/s41561-018-0089-5.

Reprints and permissions information is available at www.nature.com/reprints.

Correspondence and requests for materials should be addressed to M.M.

Publisher's note: Springer Nature remains neutral with regard to jurisdictional claims in published maps and institutional affiliations.

Methods

GPS data processing and coseismic offset estimations from time-series. Data from all available continuous GPS stations with coseismic data were compiled and processed using the Earth Parameter and Orbit System (EPOS) software[47] in the ITRF 2014 reference frame. IGS08 phase centre variations and FES2004 ocean tide loading were used with hourly tropospheric wet zenith delays estimated as random-walk parameters and Vienna mapping functions in a grid file database. The reprocessed precise satellite orbit and clock products were generated together with station coordinates by EPOS and combined with IGS products in order to reduce the impact in estimating Earth rotation parameters.

We estimated the coseismic offset of the GPS data from the continuous stations FUTF, GUAF, MELK, MUER, PMO1, PTRO, GLLN, RMBA, TPYU installed by the National Seismological Center of Chile (CSN) and the University of Potsdam, Germany. The resulting time series were automatically cleaned for all data and/or error outliers. The coseismic offset was estimated using an iterative least-square inversion that also solves for additional signal components[48,49] like the linear (interseismic) plate rate, antenna offsets, seasonal and semi-seasonal variations and coseismic offsets from relevant earthquakes in the vicinity, based on the NEIC (National Earthquake Information Center, https://earthquake.usgs.gov) earthquake catalogue and with a threshold given by the magnitude–distance relationship. The variance of the resulting coseismic offsets was estimated using the averaged data fit normalized by overall length of the time series[50]. Supplementary Figure 1 shows the time series and the parameters estimated for each station used in our analysis.

InSAR data. C-band and L-band Synthetic Aperture Radar (SAR) data acquired by the European and Japanese space agencies (ESA, JAXA), respectively, were used in this study. They include a pair of ascending and descending C-band SAR data acquired in interferometric wide-swath (IW) mode from the Sentinel-1 (S1) satellite and a pair of descending L-band SAR data acquired in ScanSAR mode (full aperture) by Advanced Land Observing Satellite 2 (ALOS 2). S1 interferograms were constructed from images acquired on 12 December 2016 and 10 January 2017 for descending and 21 December 2016 and 14 January 2017 for ascending pairs, whereas the ScanSAR ALOS-2 interferogram was constructed from images covering 1 December 2016 and 12 January 2017. The S1 interferograms were processed with the GAMMA software[51]. The spectral diversity method[52] was applied for precise coregistration of SAR data. ALOS-II ScanSAR processing[53] was done using SARscape (http://www.sarmap.ch/wp/). A 90 m digital elevation model that was derived from the NASA Shuttle Radar Topography Mission (SRTM) was used as the reference topography model[54] for the topography-related phase correction and geocoding of all the interferograms. The coseismic wrapped interferograms (Supplementary Fig. 2) were unwrapped using the minimum cost flow (MCF) method[55] (Supplementary Fig. 3).

The unwrapped data were visually checked for unwrapping errors, which were either corrected or excluded from the modelling (for example mountainous areas). We then subsampled the data using the quad-tree approach[56](Supplementary Fig. 4). In parallel, we calculated the corresponding line of sight (LOS) and the centre of mass of all valid data within one subsampled cell that was used as observation coordinate. Overall, we obtained 520 data points for the Sentinel 1 ascending data set, 550 points for the Sentinel 1 descending data set and 230 data points for the ALOS descending data set.

In the modelling, we accounted for a phase jump of a multiple of 2π between the main land, Chiloé Island and Guafo Island by introducing three additional parameters for InSAR phase ambiguities between these subsets. As the first-order proxy for estimating the noise level of the data we used the inverse of the width of the subsampled quads[57].

Slip inversion. Plate interface slip was modelled using over 600 triangular patches with a mean area of 65 km^2 meshed to represent the undulating plate interface model[58]. Slip on each patch was represented by Green's functions of dislocation in an elastic half-space[59] and two slip vectors were solved for at each patch. These two slip vectors bound the horizontal azimuthal motion of each patch between the bearings of 250 and 290 degrees. In the inversion for slip, the lower bound of slip for each slip direction was defined as zero, so that all modelled slip has a thrust component. A maximum slip for each slip direction was set at 5 m. The bounding azimuths were selected to represent a realistic direction of plate interface motion based on the focal mechanics of moment tensor inversions along this subduction margin. The inversion problem was formulated in the L2 regularization sense so that the procedure enacted the following optimization:

$$\text{minimize} \|w \times (d - G \times m)\|_2 + \beta \|m\|$$

subject to:

$$0 \leq m \leq 5$$

where d is the data vector containing the GPS, G are the Green's functions, m is the solution vector corresponding to the amounts of slip for each Green's function, w is the vector of weights for each data point, and β is the weighting of the regularization. Accordingly, this optimization is the solution of the Tikhonov damped, bounded, weighted least squares problem. Data are first weighted by their respective errors with a uniform error of the InSAR estimated to be 6 cm from the lateral variability of the data. The data are then further weighted in the inversion so that InSAR LOS data are weighted 10 times as strongly as GPS displacements. The choice of ratio between weighting of GPS and InSAR was based upon the approach of ref. [60]. The optimization was regularized with the L2 norm of the parameter values. The favoured damping coefficient was selected using a trade-off curve between model misfit and damping coefficient (Supplementary Fig. 5). The optimization was performed using the Matlab package CVX OPT[61].

Checkerboard tests were performed revealing regions of the interface that are better resolved and the sizes of kinematic heterogeneity that can be isolated (Supplementary Fig. 5). In the region containing the mainshock and aftershock seismicity, the results of the checkerboard tests confirm that the modelled slip distribution is in a relatively well resolved region of the plate interface and that the shape of the recovered slip distribution is broader than the finest scale that can be resolved.

Seismicity. We used raw waveform data from seismic networks C and C1 available on IRIS (https://ds.iris.edu/SeismiQuery/) to detect and locate aftershock seismicity after the 25 December earthquake. Initially, we ran a recursive STA/LTA trigger algorithm over the raw data and searched for events with coherent arrivals at at least five stations. After manually picking P and S phases for these events, we also visually checked the raw waveform data at station GO07 (which is closest to the main shock) and identified additional smaller events that were missed in the first step. All events that were visible on at least four seismometer stations were also handpicked and added to the dataset. This yielded a total of 262 earthquakes detected in the time interval between the main shock and 31 January 2017, nearly all of which are located in the main shock area. We also ran the STA/LTA algorithm over the two years of data preceding the main shock, but found no significant precursory activity. However, network coverage in the region has increased only recently, which means smaller events before 2015 may have been missed. For relocation, we employed joint hypocentre determination[62] to the manual P and S picks, keeping the velocity model fixed to the local model[30]. Due to the relatively small number of stations at close distances and their unfavourable geometry (most stations are located to the NE of the main shock; no coverage at western azimuths), hypocentral depths are not well defined, but epicentres should be relatively reliable.

We also determined moment tensors for five of the largest aftershocks with a previously reported technique[63]. Only these five events had sufficient signal-to-noise ratios at long periods to be thus inverted. We required the solutions to be deviatoric, and used the period band between 15 and 35 s. The epicentres for these events were fixed to their catalogue position, and inversions with different trial centroid depths were performed. The trial depth with the lowest misfit solution was then chosen as the optimal centroid depth. All five aftershocks show low-angle thrust mechanisms, and their depths are situated close to the plate interface as defined previously[58], giving us confidence that the aftershock seismicity is indeed situated on the plate interface. Since moment tensor inversion is less dependent on event–station geometry than hypocentral location, these centroid depths should be more reliable than the ones from the event catalogue. The aftershocks sequence is characterized by a rapid decay in the number of events (Supplementary Fig. 6).

Multichannel seismic reflection data. Multichannel seismic reflection data were acquired offshore of Guafo Island during the SPOC using R/V Sonne in 2000/2001. (Supplementary Fig. 7). The signals for the seismic reflection experiment were generated by a tuned set of 20 air guns with a total volume of 51.2 l. The multichannel seismic reflection data were analysed using standard processing, including re-binning, normal move out correction, stacking, deconvolution and post-stack time migration. A predictive deconvolution with two gates, for the shallow sedimentary events and the deeper crustal events, was applied before the stack.

A space and time variant frequency filter prior to a post-stack migration completed the processing flow[64]. The seismic recording system is characterized by a record length of 14,332 ms, a sampling rate of 4 ms, and a LC-Filter of 3 Hz. The shots were triggered in time intervals of 60 s on full minutes UTC. At a speed of 5 knots that results in a shot point distance of 154 m. A constant hydrophone spacing of 25 m (108 channels) was chosen for the seismic processing, resulting in a common mid-point distance of 12.5 m and a maximum fold of 27 (ref. [64]). Results of the seismic reflection processing are used to characterize the depth-varying structural features (Supplementary Fig. 7). A reflective zone shows the upper limit of the continental basement, which defines the lower limits of a sedimentary basin. Guafo Island lies in the centre of this forearc basin, which has a sediment thickness of ~750 m at its depocentre (Fig. 2b).

Mechanical modelling. The purpose of this model is to estimate the spatiotemporal evolution of stress build-up along the seismogenic zone, and its relationship to the lag time between the 1960 and 2016 earthquakes. We performed 3D geomechanical simulations using the PyLith software[65]. Our model consists of an elastic downgoing slab (oceanic plate) and an upper crustal unit (overriding continental plate) that sit on top of oceanic and continental asthenospheric units, respectively (Supplementary Fig. 8). We specified a Young's modulus of 100, 120

and 160 GPa, for the continental, oceanic and mantle layers, respectively[28]. The Poisson's ratio was set to 0.265 and 0.30 for the continental and oceanic crusts[66], respectively.

To simulate the steady interseismic subduction of the oceanic plate, we implemented the previously reported Elastic Plate Model[35]. In this model, the plate subduction is kinematically represented by the superposition of creep along the entire base of the oceanic crust and on the top of the slab below the seismogenic zone (Supplementary Fig. 8). We specified two fault interfaces with kinematic fault conditions, representing the base of the slab (Fault3) and the creeping part below the seismogenic zone (Fault2). On those interfaces, we prescribed a homogeneous constant creeping equal to the plate convergence velocity (6.6 cm yr^{-1}), but with opposite sense of movement. The seismogenic fault (Fault1) extends between 0 and 30 km depth and is divided at 20 km depth into two segments (the shallower and deeper seismogenic segments) with different coefficients of effective friction (Fig. 2). The frictional behaviour of the seismogenic zone is modelled with the Coulomb failure criterion:

$\tau = \mu' \times (\sigma_n') + c$, where τ is the shear strength of the fault, μ' is the effective friction coefficient, σ_n' is the fault normal stress and c is the cohesion. Here, fault activation occurs when the driving forces exceed τ. For simplicity, our model neglects gravity body force but specifies normal tractions consistent with overburden (lithostatic load) as initial stress state along the frictional fault. We simulate the mechanical behaviour of a coupled asperity by clamping a section of the fault, so that it has a higher friction than the non-asperity region of the fault.

In our mechanical model, tectonic forces (slab pull) load the system and fault strength controls the levels of stress that the fault can support before sliding. We do not model the complex dynamics of rupture nucleation, dynamic interaction between asperities, or rupture propagation. Rather, we focus on the static friction that needs to be overcome to begin the process of fault motion, and not the subsequent evolution of material properties during a seismic event. Therefore, our model contributes to the conceptual understanding into the level of stress that the seismogenic zone can support before breaking in medium to large earthquakes. Other significant assumptions we make include: (i) the stress drops in the earthquakes must represent almost all of the pre-earthquake shear stress on the faults, and so the faults must be able to support only a few tens of megapascals of shear stress before slipping in earthquakes; (ii) the 1960 earthquake totally released the stress in the 2016 rupture zone; (iii) frictional strength is uniform along-strike in the study area.

We tested different values of the effective friction coefficient for both fault segments; running a total time of 360 yr of steady interseismic loading. We define the onset of instable fault behaviour as the rupture time. In this study, we assumed that the fault instable behaviour occurs when the fault creep rate exceeds 3 cm yr^{-1}. We also varied this threshold value between 1 and 5 cm yr^{-1} and found that this variation does not significantly impact the retrieved rupture times.

Supplementary Fig. 10 shows the rupture times of all tested effective friction coefficient combinations for the two segments. Results indicate that both segments must be weak with a low coefficient of effective friction (generally <0.1) to maintain a reasonable rupture time (generally <300 yr), which is consistent with previous studies[18,67]. These results give a range of friction combinations that produces rupture of the deeper segment after 56 yr of loading (Supplementary Fig. 10). For the deep segment to rupture at 60 ± 5 yr (black circles in Supplementary Fig. 10b), the rupture time of shallow segment depends on the ratio of the effective friction coefficients between the two segments.

We estimated the change of Coulomb failure stress (CFS)[68] predicted by our optimal slip distribution (Supplementary Fig. 12). We use a homogeneous coefficient of friction $\mu = 0.5$ (ref. [69]). The CFS values (<1.5 MPa) are in keeping with those expected from such a moderate size earthquake. We estimate the optimal range effective friction coefficient combinations that induce accumulation of stress build-up similar to the stress drop at the 2016 rupture zone, and use this frictional ratio to estimate the rupture time of the shallow segment. In order to accumulate shear stresses in the range of the stress drop of the 2016 event, the effective friction coefficient of the deep segment has to be 30–40% of the value of the shallow segment (Fig. 4a). For this friction coefficient combination, the shallow segment fails after 110–140 yr of loading.

The low effective friction coefficients of our model can be interpreted to be the result of high pore fluid pressure. High pore fluid pressure acts to locally reduce the effective normal stress on faults, which are able to fail at lower shear stresses than if the fluid were absent[10].

The effective friction coefficient $\mu' = \mu_0 \times (1-\lambda)$, can be used to incorporate pore pressure into the Coulomb stress criterion, where μ_0 is a typical frictional sliding coefficient and the value of λ, so-called the pore pressure ratio, represents the degree to which pore pressure counteracts the total stress generated by the overburden stress. Considering the typical frictional sliding coefficient as 0.5 in southern Chile subduction zone[69], we derived the pore pressure ratio of the two segments by the formula of $\lambda = 1-\mu'/\mu_0$. Figure 4b shows the parameter space of λ of the two segments that allows the deep segment ruptures after a reasonable amount of time. For the deep segment, λ has to be >0.98 to permit its rupture after 56 years of loading. It is expected that in the shallow segment $\lambda \simeq 0.95$–0.96 in order to accumulate shear traction matching the stress drop of the 2016 event.

Stress anomaly. To gain insight into the heterogeneity of the initial static stress distribution at the plate interface we make use of normal stress anomalies reported previously[70]. The anomaly is derived from vertical stress (lithostatic load) and then projected into the normal of the subduction interface. Since there is no external horizontal component involved, it is more exactly expressed as normal component of the vertical stress anomaly. Using a 3D density model further developed from the gravity forward modelling reported previously[71], the vertical stress effects of density anomalies at the computation depth, that is the interface of the subducting plate in the 3D model, are incorporated into the model. Density anomalies are defined as bodies of a rock density that deviate from the standard three-layer reference model used during gravity forward modelling of the 3D density model. Isostatic or flexural effects are not considered. Topographic masses add to the vertical load and therefore we added the lithostatic stress effect of topographic masses by using ETOPO1 heights and a standard density of 2,670 kg m^{-3}. The sum of the results in the vertical component is then projected into the interface normal. The static stress anomaly grid was computed on a ~3 minutes grid. For the 3D model, therefore, normal stresses are carefully calculated.

Our mechanical clamping models indicate that including the normal stress anomaly (due to density contrast in the forearc) (Supplementary Fig. 14), with a constant value for the effective friction coefficient, cannot produce the coupling pattern of the asperity (Supplementary Fig. 15) and therefore variations of effective friction along the plate interface are needed to clamp the fault.

Code availability. Numerical simulations were calculated in Pylith[65], which is available on the Computational Infrastructure for Geodynamics web site (https://geodynamics.org/cig/software/pylith/). Codes developed in this study to simulate stress build-up under interseismic loading are available from the corresponding author upon reasonable request. The GAMMA and SARScape software used to compute the interferograms can be accessed at www.gamma-rs.ch and www.sarmap.ch/page.php?page=sarscape, respectively.

Data availability. The GPS data that support the findings of this study are available in the GNSS data repository of the Centro Sismologico Nacional, Chile (http://gps.csn.uchile.cl/data/). GPS data from stations GUAF and MELK (before 2016) are available from the corresponding author upon reasonable request. C-band Synthetic Aperture Radar imaging from the Sentinel mission is available from the Copernicus Open Access Hub (https://scihub.copernicus.eu). ALOS original data are copyright to the Japanese Aerospace Exploration Agency and are not publicly available.

References

47. Deng, Z., Gendt, G. & Schöne, T. in *IAG 150 Years* Vol. 143 (eds Rizos, C. & Willis, P.) 33–40 (Springer, Cham, 2015).
48. Metzger, S. et al. Present kinematics of the Tjörnes Fracture Zone, North Iceland, from campaign and continuous GPS measurements. *Geophys. J. Int.* **192**, 441–455 (2013).
49. Bevis, M. & Brown, A. Trajectory models and reference frames for crustal motion geodesy. *J. Geod.* **88**, 283–311 (2014).
50. Geirsson, H. et al. Current plate movements across the Mid-Atlantic Ridge determined from 5 years of continuous GPS measurements in Iceland. *J. Geophys. Res.* **111**, B09407 (2006).
51. Wegmuller, U. & Werner, C. Gamma SAR processor and interferometry software. In *3rd ERS Symp. Space Serv. Environ.* (eds Guyenne, T. D. & Danesy, D.) 1687–1692 (ESA, Noordwijk, 1997).
52. Scheiber, R. & Moreira, A. Coregistration of interferometric SAR images using spectral diversity. *IEEE Trans. Geosci. Remote Sens.* **38**, 2179–2191 (2000).
53. Guarnieri, A. & Prati, C. Scansar focusing and interferometry. *IEEE Trans. Geosci. Remote Sens.* **34**, 1029–1038 (1996).
54. Farr, T. & Kobrick, M. Shuttle radar topography mission produces a wealth of data. *Eos Trans. Am. Geophys.* **81**, 583–585 (2000).
55. Costantini, M. A novel phase unwrapping method based on network programming. *IEEE Trans. Geosci. Remote Sens.* **36**, 813–821 (1998).
56. Jónsson, S., Zebker, H., Segall, P. & Amelung, F. Fault slip distribution of the 1999 M_w 7.1 Hector Mine, California, earthquake, estimated from satellite radar and GPS measurements. *Seismol. Soc. Am. Bull.* **92**, 1377–1389 (2002).
57. Sudhaus, H. & J¢nsson, S. Improved source modelling through combined use of InSAR and GPS under consideration of correlated data errors: application to the June 2000 Kleifarvatn earthquake, Iceland. *Geophys. J. Int.* **176**, 389–404 (2009).
58. Tassara, A. & Echaurren, A. Anatomy of the Andean subduction zone: three-dimensional density model upgraded and compared against global-scale models. *Geophys. J. Int.* **189**, 161–168 (2012).
59. Okada, Y. Internal deformation due to shear and tensile faults in a half-space. *Bull. Seism. Soc. Am.* **82**, 1018–1040 (1992).
60. Cavalie, O. et al. Slow slip event in the Mexican subduction zone: evidence of shallower slip in the Guerrero seismic gap for the 2006 event revealed by the joint inversion of InSAR and GPS data. *Earth Planet. Sci. Lett.* **367**, 52–60 (2013).

61. Grant, M. C. & Boyd, S. P. in *Recent Advances in Learning and Control* (eds Blondel, V. et al.) 95–110 (Springer, London, 2008).
62. Kissling, E., Ellsworth, W. L., Eberhart-Phillips, D. & Kradolfer, U. Initial reference models in local earthquake tomography. *J. Geophys. Res.* **99**, 19635–19646 (1994).
63. Nabelek, J. & Xia, G. Moment-tensor analysis using regional data: application to the 25 March, 1993, Scotts Mills, Oregon, Earthquake. *Geophys. Res. Lett.* **22**, 13–16 (1995).
64. Reichert, C., Schreckenberger, B. & SPOC Team. *Fahrtbericht SONNE-Fahrt SO-161 Leg 2 and 3 SPOC -Subduktionsprozesse vor Chile- BMBF-Forschungsvorhaben 03G0161A* Valparaiso 16.10.2001–Valparaiso 29.11.2001 (Bundesanst. für Geowis. und Rohstoffe, 2002).
65. Aagaard, B., Knepley, M. & Williams, C. A domain decomposition approach to implementing fault slip in finite-element models of quasi-static and dynamic crustal deformation. *J. Geophys. Res.* **118**, 3059–3079 (2013).
66. Christensen, N. Poisson's ratio and crustal seismology. *J. Geophys. Res.* **101**, 3139–3156 (1996).
67. Li, S., Moreno, M., Rosenau, M., Melnick, D. & Oncken, O. Splay fault triggering by great subduction earthquakes inferred from finite element models. *Geophys. Res. Lett.* **41**, 385–391 (2014).
68. King, G. P., Stein, R. & Lin, J. Static stress changes and the triggering of earthquakes. *Bull. Seismol. Soc. Am.* **84**, 935–953 (1994).
69. Lamb, S. Shear stresses on megathrusts: Implications for mountain building behind subduction zones. *J. Geophys. Res.* **111**, B07401 (2006).
70. Gutknecht, B. D. et al. Structure and state of stress of the Chilean subduction zone from terrestrial and satellite-derived gravity and gravity gradient data. *Surv. Geophys.* **35**, 1417–1440 (2014).
71. Tassara, A., Götze, H., Schmidt, S. & Hackney, R. Three-dimensional density model of the Nazca plate and the Andean continental margin. *J. Geophys. Res.* **111**, B09404 (2006).